2021

Trabecular Bone Organoid Model for Studying the Regulation of Localized Bone Remodeling

Yongkuk Park

Eugene Cheong

Jun-Goo Kwak

Ryan Carpenter

Jae-Hyuk Shim

See next page for additional authors

Authors

Yongkuk Park, Eugene Cheong, Jun-Goo Kwak, Ryan Carpenter, Jae-Hyuk Shim, and Jungwoo Lee

APPLIED SCIENCES AND ENGINEERING

Trabecular bone organoid model for studying the regulation of localized bone remodeling

Yongkuk Park[1], Eugene Cheong[2], Jun-Goo Kwak[3], Ryan Carpenter[1], Jae-Hyuck Shim[4], Jungwoo Lee[1,3]*

Trabecular bone maintains physiological homeostasis and consistent structure and mass through repeated cycles of bone remodeling by means of tightly localized regulation. The molecular and cellular processes that regulate localized bone remodeling are poorly understood because of a lack of relevant experimental models. A tissue-engineered model is described here that reproduces bone tissue complexity and bone remodeling processes with high fidelity and control. An osteoid-inspired biomaterial—demineralized bone paper—directs osteoblasts to deposit structural mineralized bone tissue and subsequently acquire the resting-state bone lining cell phenotype. These cells activate and shift their secretory profile to induce osteoclastogenesis in response to chemical stimulation. Quantitative spatial mapping of cellular activities in resting and activated bone surface coculture showed that the resting-state bone lining cell network actively directs localized bone remodeling by means of paracrine signaling and cell-to-cell contact. This model may facilitate further investigation of trabecular bone niche biology.

INTRODUCTION

Trabecular bone is a dynamic, multifunctional tissue that regulates mineral homeostasis, blood-forming, and mechanical structure in response to changing physical stresses and physiological needs (*1*, *2*). Trabecular bone undergoes repeated remodeling by the paired action of osteoclasts, which break down bone, and osteoblasts, which form new bone (*3*). During active bone remodeling, osteoblasts build osteoids, collagen-based structures of extracellular matrix (ECM) that they then mineralize to form new lamellar bone (*3*). After an osteoid has been mineralized, osteoblasts on the bone surface differentiate into their resting state: bone lining cells (*3*). The cellular processes of the bone remodeling cycle occur at localized spots under tight regulation by stimulatory and suppressive molecules such as receptor activator of nuclear factor κB ligand (RANKL) and its soluble decoy receptor, osteoprotegerin (OPG) (*4*). RANKL stimulates bone marrow mononuclear cells (BMMs) to differentiate into osteoclasts by binding to its receptor, RANK, whereas OPG blocks RANK-RANKL signaling by competitively binding to RANKL and thus suppressing osteoclast differentiation (*4*).

Active- and resting-state bone tissue surfaces coexist within every bone. There are 1 million active remodeling sites in a normal adult skeleton at any one time, which account for 5 to 20% of the total bone surface (*5*, *6*). Molecular regulation is essential to localize bone remodeling activity and prevent unnecessary remodeling and overresorption. Imbalanced bone remodeling can lead to osteoporosis (*7*), decreased bone marrow hematopoietic activity (*8*), or increased risk of bone metastasis (*9*). To develop effective treatments for these conditions, it is imperative that we understand how localized bone remodeling is regulated in the trabecular bone cavities.

Spatiotemporal profiles of regulatory molecules may play a critical role in directing localized bone remodeling activity. In normal bone remodeling, trabecular bone undergoes continuous structural change but maintains consistent morphology and mass (*10*). This implies that localized bone remodeling is in part regulated by bone turnover rate and morphology. Countergradients of stimulative and inhibitory molecules are key regulatory mechanisms in localized morphogenic activity that direct the size and shape of tissue development and regeneration (*11*, *12*). We postulate that the same principle applies to the regulation of trabecular bone remodeling. Osteoblasts secrete both stimulative and suppressive molecules, and their secretory profiles change depending on whether they are in an active or a resting state (*13*). Secreted regulatory molecules form diffusion gradients as a function of the diameters of the trabecular bone cavities (*14*). Therefore, key determinants of the spatiotemporal profile of regulatory molecules in trabecular bone cavities are the extent of remodeling activity and the cavity diameter. To investigate this concept in more detail, a new experimental model is needed.

Available experimental models have limited ability to reproduce the spatiotemporal complexity of trabecular bone. Mouse models have limited utility to investigate cellular and molecular processes of trabecular bone remodeling because the inner bone surface is anatomically inaccessible and researchers have limited ability to manipulate the structure and dimensions of the trabecular bone. Explanted bone chips are more accessible, but local manipulation of cellular metabolic activity and dimensional control of bone are limited, and reproducibility is low because tissue dimensions are variable and vascular occlusion decreases cell viability over time (*15*).

In vitro bone tissue models allow greater experimental control and access, and many biomaterials and material-processing techniques have been introduced to reproduce the material and structural properties of bone ECM in in vitro bone tissue models (*16*). However, existing in vitro models do not reproduce the bone tissue complexity and molecular and cellular processes of bone remodeling (*17*). For example, compact bone disks have been used to assess osteoclasts function (*18*) and demineralized trabecular bones have been used to culture osteoblasts (*19*). However, grinding compact bone is burdensome and low throughput, and the opacity of bone restricts in situ optical microscopy. Demineralized trabecular bone supports high osteogenic activity (*19*), but its three-dimensional (3D) architecture

[1]Department of Chemical Engineering, Institute for Applied Life Sciences, University of Massachusetts, Amherst, MA 01003, USA. [2]Department of Biochemistry and Molecular Biology, University of Massachusetts, Amherst, MA 01003, USA. [3]Molecular and Cellular Biology Graduate Program, University of Massachusetts, Amherst, MA 01003, USA. [4]Department of Medicine, University of Massachusetts Medical School, Worcester, MA 01655, USA.
*Corresponding author. Email: jungwoo@umass.edu

is determined by the individual bone matrix and is difficult to standardize or manipulate for mechanistic investigation. Collagen gels provide a biochemical milieu comparable to that of bone ECM but fail to reproduce the density and structural organization of collagen fibers (*20*). Hydroxyapatites mimic inorganic aspects of bone ECM but lack the organic materials that are known to provide biochemical signals (*16*). Blends of organic and inorganic materials better represent bone ECM but do not provide multiscale structural complexity (*16*). Techniques have been developed to produce nanoscale surface roughness, microscale pore geometry, and macroscale trabecular architecture in biomaterials—including porogen-based porous architecture, electrospun fibrous meshwork, and 3D-printed trabecular bone structure (*21*)—but these processes do not recapitulate the hierarchical composite structures of trabecular bone in the critical dimensions of lamellae (5 to 25 µm), collagen fibers (1 to 2 µm), and collagen fibrils (10 to 300 nm) (*20*). In addition, most in vitro biomaterial studies have focused on either osteoblasts or osteoclasts, but few studies have involved osteoblasts and osteoclasts in coculture (*22*, *23*). In the body, active osteoblasts and osteoclasts are only present transiently at local spots, while most of the bone surface is in a quiescent state characterized by bone lining cells (*6*). The role of bone lining cells in the initiation and termination of the bone remodeling cycle has not been investigated, and failures in initiation or termination of the bone remodeling cycle could be a critical factor in bone remodeling imbalance.

Here, we report the development of a trabecular bone organoid model that reproduces essential extracellular complexity and cellular processes of trabecular bone cavities. We reproduced unmineralized bone ECM—the osteoid—with thin slices of demineralized cortical bone. This material is mechanically durable, semitransparent, and has controlled thickness and surface area. We named this biomaterial demineralized bone paper (DBP). We explored whether DBP directs osteoblasts to form mineralized bone tissue and acquire the bone lining cell phenotype. We then cocultured primary murine osteoblasts and BMMs and applied chemical stimulants to reproduce the bone remodeling cycle. We created defined spatiotemporal profiles of regulatory molecules by combining DBP surfaces containing active- and resting-state osteoblasts. Last, we conducted quantitative spatial mapping of cellular activities to investigate how localized bone remodeling activity is regulated. We expect that the trabecular bone organoid model will facilitate further study of the complex and dynamic regulation of bone remodeling processes with high fidelity and an unprecedented level of analytical power.

RESULTS

DBP effectively simulates the trabecular osteoid

To reproduce the bone remodeling process in a controlled and analytical manner, we developed a biomaterial that mimics the dense structural collagen matrix of the unmineralized osteoid with thin sections of demineralized bovine compact bone. First, we established a method to rapidly demineralize bone matrix. We cut bovine femurs into 4- to 5-cm blocks, removed marrow and connective tissue, and dissolved the fat in methanol and chloroform. Then, we submerged the blocks in 1.2 N hydrochloric acid to dissolve bone mineral. The outer layer of bone turned semitransparent after 5 days, but demineralization progressed little over the next 4 weeks because diffusion through the dense collagen matrix was limited (Fig. 1A). Under the hypothesis that cyclic hydrostatic pressure can promote

the demineralization process, we devised a programmable pressure chamber operated with compressed air (Fig. 1B and fig. S1). We found that demineralization depth increased when hydrostatic pressure was applied and increased further when hydrostatic pressure was applied in a cyclic pattern. The most effective operating condition was 4 bar pressure with a 10-s on/off interval. This process demineralized 5.1 ± 0.3 mm compact bone matrix in 5 days (Fig. 1C and fig. S2). Radiographic images confirmed that the processed bone tissue was fully demineralized (Fig. 1D).

We then cryosectioned a demineralized compact bone block to generate 3 × 4–cm slices and biopsy-punched the slices to obtain disks that will fit in multiwell plates (Fig. 1E). We found that 20 µm is a practical thickness that provides 80% of the light transmittance of tissue culture plate (TCP) yet retains sufficient mechanical durability for handling (stiffness: 6.5 ± 0.4 kPa) (Fig. 1F). Transmission micrographs confirmed a well-preserved bony ECM structure that exhibited distinct morphology depending on sectioning direction: Vertical sections had parallel lamellar structure, and transverse sections had concentric lamellar layers. Scanning electron microscopy (SEM) showed densely aligned collagen fiber bundles (Fig. 1G). Collagen-hybridizing peptides (CHPs) that specifically bind to damaged collagen fibrils (*24*) did not bind to demineralized bone slices. In addition, multiphoton second harmonic imaging that visualizes intact fibrillar collagen structure (*25*) revealed aligned collagen fibers (Fig. 1H). These results indicate the preserved biochemical integrity of the collagen. Last, we removed residual cellular materials from demineralized bone sections by treating with sodium dodecyl sulfate (Fig. 1I). We named these sheets of demineralized bone matrix DBP.

DBP directs rapid and structural mineralization by osteoblasts

To monitor long-term cellular processes on DBP, we collected osteoblasts from DsRed reporter mice by gently crushing femoral and tibial bones and treating the bone chips with collagenase (Fig. 2A and movie S1). We used TCP as a control substrate for DBP. Although TCP lacks bone-relevant ECM, it is similar to DBP in that it supports reproducible and analytical osteogenic cell culture experiments because it is standardized, bioactive, and has optical transparency. Osteoblasts cultured on vertically sectioned DBP for 3 days developed elongated morphology aligned with the underlying lamellar structure of the demineralized bone (±4.9°), whereas osteoblasts cultured on TCP had irregular shape and inconsistent alignment (±25.6°) (Fig. 2B and movie S2). Multiphoton second harmonic imaging microscopy showed that osteoblasts on DBP deposited collagen fibers that were directionally aligned with the lamellar structure of the bone (±7.3°), whereas those cultured on TCP had irregular collagen fiber alignment (±26.2°) (Fig. 2C and movie S3). SEM imaging further confirmed that osteoblasts on DBP deposit collagen fibers directionally (fig. S3).

Next, we characterized mineralization by osteoblasts in osteogenic differentiation medium. Time-course images with alizarin red mineral stain showed that osteoblasts on DBP completely covered the surface after 4 days and continued to deposit minerals for more than 2 weeks. In the same time period, osteoblasts on TCP deposited collagen but deposited minerals in only a few localized regions (Fig. 2D). We then conducted fluorochrome calcein staining to characterize mineral deposition patterns. On DBP, mineral deposition began with small granules embedded in the preexisting collagen matrix that gradually grew and developed into a mineralized layer (fig. S4). In
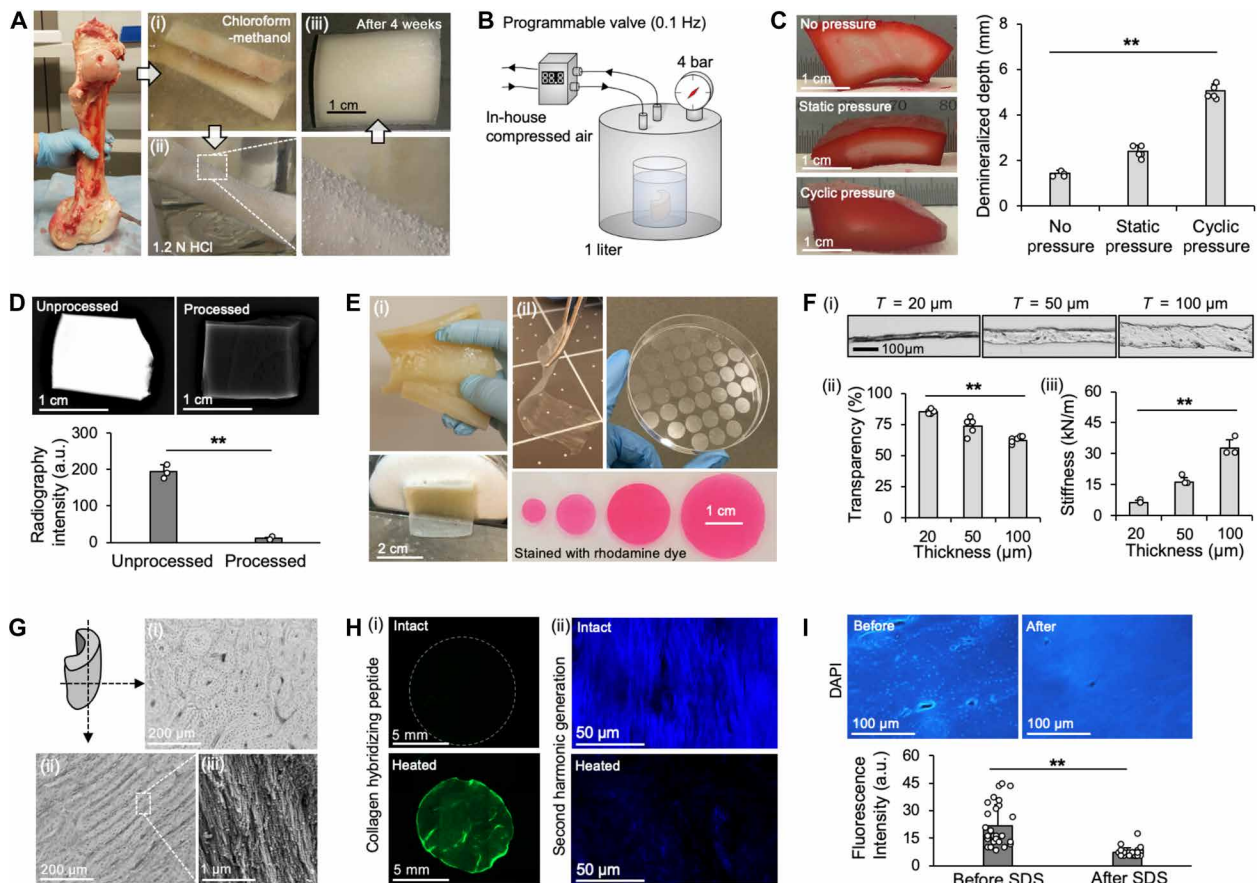
Fig. 1. Development and characterization of DBP. (**A**) A bovine femur was cut into blocks, (i) cleaned, and (ii) demineralized in HCl solution. (iii) Demineralization was limited by the diffusion limit. (**B**) We accelerated demineralization with a programmable cyclic pressure chamber. (**C**) Cross-sectional images of the bones processed in three different conditions and soaked in rhodamine dye show demineralization depth ($n = 5$). (**D**) Radiographs of processed and unprocessed bone blocks confirmed full demineralization ($n = 3$). (**E**) (i) Demineralized bone was sectioned into 20- to 100-μm slices to form DBP and (ii) cut into disks that fit multiwell plates. (**F**) (i) Cross sections of DBP with three thicknesses and corresponding (ii) optical transparency [percentage that of tissue culture plate (TCP)] and (iii) stiffness ($n = 6$). (**G**) DBP preserves the micro/nano collagen structure of bone. (i) Transverse-sectioned DBP has concentric lamellae and (ii) vertically sectioned DBP has parallel lamellae and (iii) densely aligned collagen fibril bundles [scanning electron micrographs (SEM)]. (**H**) Biochemical integrity of collagen is preserved versus heat-denatured control. (i) Fluorescent collagen hybridizing peptide stained images; (ii) multiphoton second harmonic generation images. (**I**) Removal of cellular materials by SDS was confirmed by nuclear 4′,6-diamidino-2-phenylindole (DAPI) staining ($n = 30$) (a.u., arbitrary units; *$P < 0.05$, **$P < 0.01$). Photo credit: Yongkuk Park, University of Massachusetts Amherst.

contrast, on TCP, mineral deposition occurred at local spots where clusters of osteoblasts formed mineralized nodules. Cross-sectional confocal imaging revealed that, on DBP, most mineral deposition occurred beneath osteoblasts (Fig. 2E). After 3 weeks of culture on 100-μm-thick DBP, osteoblasts typically mineralized to a depth of 18.6 ± 3.8 μm (Fig. 2F). Last, we characterized the deposited mineral structure without organic components via thermal decomposition. Cell-derived mineral layers exhibited long-range crystalline-like morphology. By contrast, mineral layers that were only formed chemically with simulated body fluid (SBF) had a disorganized structure (Fig. 2G). SEM showed that cell-derived mineral had densely fused, smooth mineral layers, whereas chemically formed mineral layers exhibited coarse aggregation of mineral granules (Fig. 2H). The characteristic surface roughness of chemically formed mineral layers was 2.3-fold higher than that of mineral layers formed by osteoblasts (fig. S5). These results indicate that DBP directs osteoblasts to proceed with rapid and structural mineralization similar to that seen in in vivo osteoid bone (*20*, *26*).

Osteoblasts on DBP acquire the bone lining cell phenotype

We investigated whether DBP can direct osteoblasts to acquire the bone lining cell phenotype and associated cellular organization and communication (*27*). Osteoblasts seeded on DBP decreased migration and proliferation over time. After they were cultured for 2 weeks, osteoblasts on DBP showed twofold decreased motility (157 ± 15 μm/day), whereas those on TCP maintained high motility (309 ± 29 μm/day) (Fig. 3A). Immunofluorescent staining of 1-week cultures with mitogenic marker Ki67$^+$ showed four times down-regulated proliferation on DBP but three times up-regulated mitogenic activity on TCP (Fig. 3B). We then examined whether osteoblasts cultured on DBP develop functional gap junctions. Immunofluorescent staining confirmed that osteoblasts express connexin 43, a key molecule in gap junction (*28*). Gap junction–mediated cellular communication was further confirmed by time-lapse fluorescent imaging of Ca^{2+}, which showed sequential Ca^{2+} influx to adjacent bone lining cells under potassium stimulation (Fig. 3C and movie S4). These data confirm that osteoblasts cultured on DBP for 1 week take on the
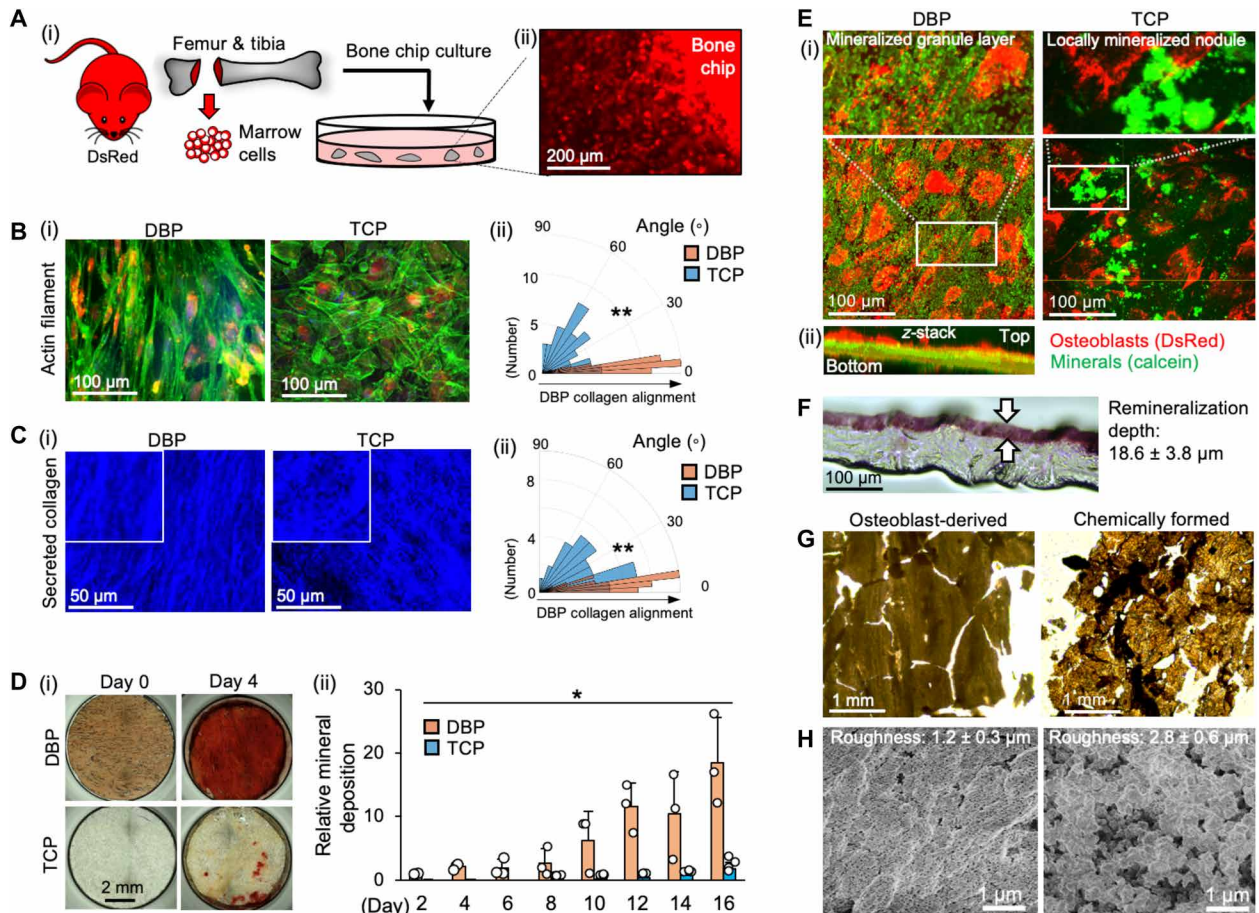
Fig. 2. Osteoblasts rapidly mineralize DBP in a way that preserves the underlying lamellar structure. (**A**) (i) Osteoblasts (OBs) harvested from DsRed mice. (ii) Fluorescent micrograph of OBs migrating out from mouse bone chips. (**B**) Morphology of OBs grown on vertically sectioned DBP and TCP for 1 week: (i) immunofluorescent staining of actin filaments; (ii) circular histogram of cell alignment angles ($n = 100$). (**C**) Collagen deposition by OBs on DBP and TCP for 1 week: (i) multiphoton second harmonic generation (SHG) images; (ii) circular histogram of collagen fiber alignment angles ($n = 100$). (**D**) Mineral deposition by OBs on DBP and TCP: (i) alizarin red mineral stain on days 0 and 4; (ii) time-course measurement of mineral deposition for 16 days ($n = 3$). (**E**) (i) Confocal images of fluorescent calcein staining show mineral deposition pattern on DBP and TCP after 1-week culture. (ii) z-staked cross-sectional image. (**F**) Cross section of 100-μm-thick DBP stained with alizarin red after 3-week culture of OBs ($n = 3$). (**G** and **H**) Comparison of the mineral layer deposited by 3-week culture of OBs and chemical reaction in simulated body fluid without OBs (both subjected to thermal decomposition): (G) bright-field micrographs. (H) SEM and surface roughness quantified by optical profiler ($n = 6$) (*$P < 0.05$, **$P < 0.01$). Photo credit: Yongkuk Park, University of Massachusetts Amherst.

bone lining cell phenotype. Hereafter, we will refer to osteoblasts that have been cultured on DBP for more than 1 week as bone lining cells.

We developed two functional assays to determine whether cells that have taken on the bone lining cell state can regain osteogenic activity. First, we developed a bone surface healing assay. We scratched the surface of DBP containing bone lining cells and monitored the subsequent activation of lining cells and increase in surface coverage. Time-lapse imaging over 5 days showed that migratory activity of bone lining cells increased transiently and then gradually returned to a resting state as the damaged area became completely confluent (Fig. 3D and movie S5). Second, we developed an osteoblast phenotypic switching assay. We released established bone lining cells from DBP by degrading the DBP with collagenase. We then cultured the released cells on TCP and found that they resumed their migratory and proliferative activity (movie S6). Quantitative analysis of Ki67+ cells confirmed that bone lining cells released from DBP and cultured on TCP for 1 week recovered mitogenic activity comparable to that of osteoblasts that were continuously cultured on TCP (Fig. 3E).

When the TCP-expanded osteoblasts were detached and reintroduced onto DBP, they regained the bone lining cell phenotype. This cycle of phenotypic switching from resting to active states by alternating DBP and TCP substrates was repeated at least three times. With each cycle, the time required to reach 80% confluency on TCP increased: 8 days in the first cycle, 15 days in the second cycle, and 30 days in the third cycle. Alizarin red staining showed that mineral deposition activity was similar in each of the three cycles (Fig. 3F). These data indicate that cells that take on the bone lining cell phenotype on DBP retain the ability to revert to active state osteoblasts, as they would in the bone remodeling cycle in vivo (*3, 29*).

The microenvironment of DBP supports the bone remodeling cycle

Bone remodeling begins when chemical or mechanical stimulation triggers a shift in the local profile of osteogenic regulatory molecules that induces BMMs to differentiate into osteoclasts. When stimulation ceases, up-regulated stimulatory molecules return to resting levels
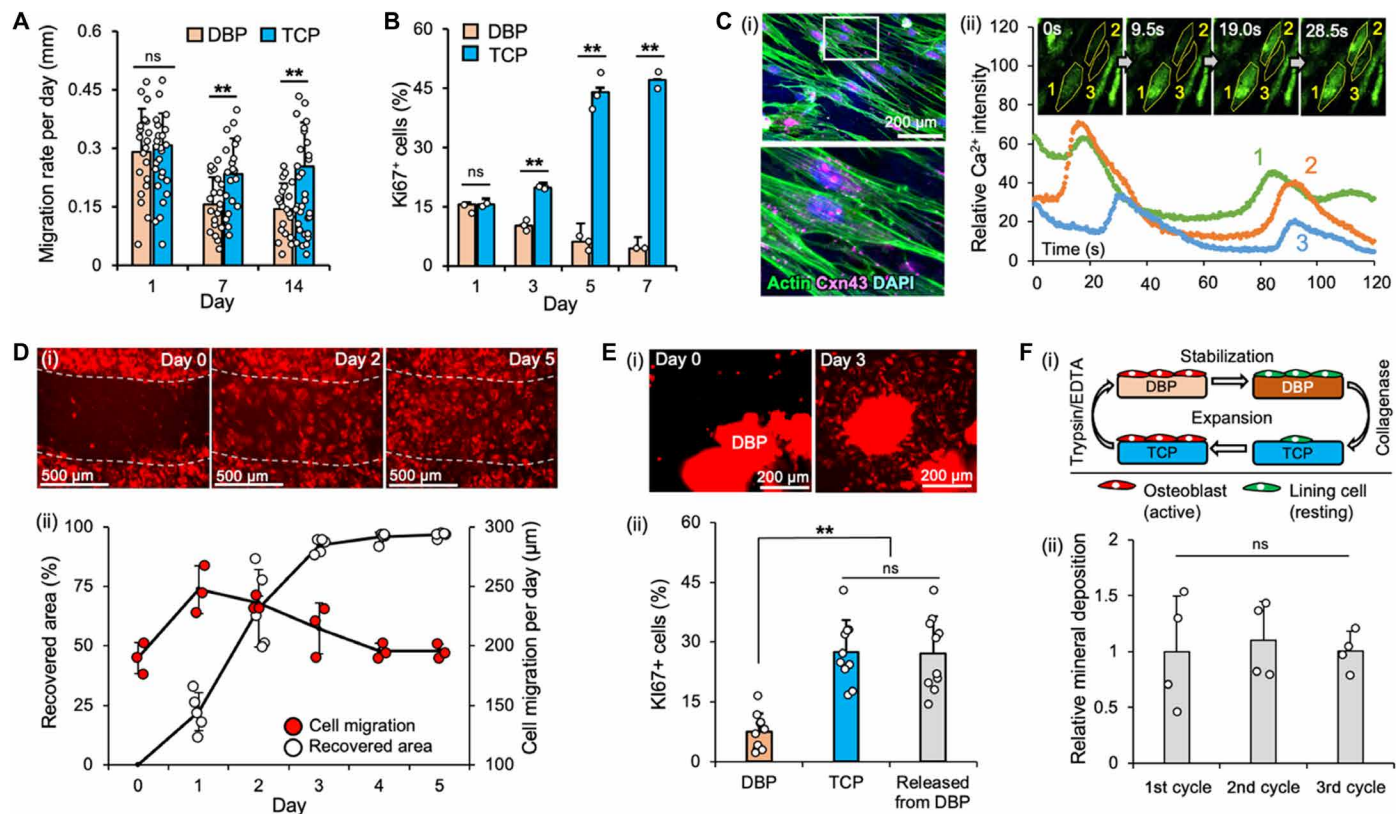
Fig. 3. OBs on DBP acquire the bone lining cell phenotype. (**A**) OBs on DBP migrated more slowly than those on TCP ($n = 25$). (**B**) OB on DBP proliferated less than those on TCP ($n = 3$). (**C**) OBs on DBP developed gap junction–mediated intercellular communication. (i) Immunofluorescent staining of connexin 43. (ii) Time-lapse monitoring of fluorescent Ca^{2+} flux in adjacent cells. (**D**) Bone surface healing assay: (i) Repair of mineral surface was monitored after scratch in 1-week culture of OBs on DBP; (ii) quantitative measurement of transiently increased OB migration during healing process ($n = 3$ to 5). (**E**) OBs cultured on DBP for 1-week regained proliferative activity when cultured on TCP. (i) Fluorescent images of mature OBs migrating out of DBP treated with collagenase and proliferating on TCP. (ii) Within 1 week, mature OBs released from DBP and grown on TCP regained mitogenic activity similar to that of OBs grown continuously on TCP ($n = 10$). (**F**) OB phenotypic switching assay: (i) experimental procedure and metabolic state changes in OBs. (ii) The cycle of switching from resting state on DBP to proliferative state on TCP was successfully repeated three times ($n = 4$) (*$P < 0.05$, **$P < 0.01$, ns, not significant).

and bone remodeling terminates (*3*). To reproduce the activation of a bone remodeling cycle, we stimulated bone lining cells on DBP to become active and then added BMMs to see whether the BMMs differentiated into osteoclasts and initiated bone remodeling (Fig. 4A). First, we used enzyme-linked immunosorbent assays to measure the profiles of representative stimulative and suppressive molecules—RANKL and OPG—secreted by bone lining cells on DBP. The bone lining cells secreted high OPG (12.7 ± 0.5 ng/ml) and low RANKL (0.09 ± 0.001 ng/ml). The ratio of OPG to RANKL was 0.007, which indicates a highly suppressive molecular milieu for the initiation of bone remodeling cycle. We then examined whether bone lining cells on DBP change their secretory profile when exposed to chemical instigators of bone remodeling, vitamin D3 (VD3) and prostaglandin E2 (PGE2) (*22*). When exposed to a physiological range of VD3 (10 nM) and PGE2 (1 µM), the secretion profile of the bone lining cells markedly shifted: OPG decreased sixfold and RANKL increased 30-fold. The shifted RANKL/OPG ratio was 1.47, which indicates a permissive molecular niche for bone resorption. Without additional stimulation, the secretion profile gradually returned to the initial resting state in 1 week (Fig. 4B). In contrast, osteoblasts on TCP secreted moderate levels of OPG (1.6 ± 0.02 ng/ml) and RANKL

(1.1 ± 0.04 ng/ml) at a ratio of 0.65, nearly 100 times higher than the ratio secreted by bone lining cells on DBP. VD3 and PGE2 stimulation also shifted the secretory profile of osteoblasts on TCP to a RANKL/OPG ratio to 34.2. After stimulation, the cells on TCP returned to the initial state of molecular secretion more slowly than did those on DBP (fig. S6).

Next, we examined whether the up-regulated secretion of stimulatory molecules by activated bone lining cells on DBP can induce BMMs to differentiate into osteoclasts. We used green fluorescent protein (GFP)–expressing osteoblasts and DsRed-expressing BMMs to facilitate long-term, time-lapse fluorescent monitoring of multicellular processes in the DBP. We stimulated established bone lining cells with VD3 and PGE2 and cocultured them with 1×10^6 BMMs. After 1 week, multinucleated osteoclasts began to appear (Fig. 4C and movie S7). SEM showed localized removal of the mineral layer and exposure of the collagen fibers underlying osteoclasts, confirming functional osteoclasts (Fig. 4D). These results indicate that shifted secretion of regulatory molecules was sufficient to induce BMMs to differentiate into osteoclasts that resorbed mineral. We repeated the process on TCP for comparison and found that osteoclasts began to emerge on TCP after 3 days (movie S8).
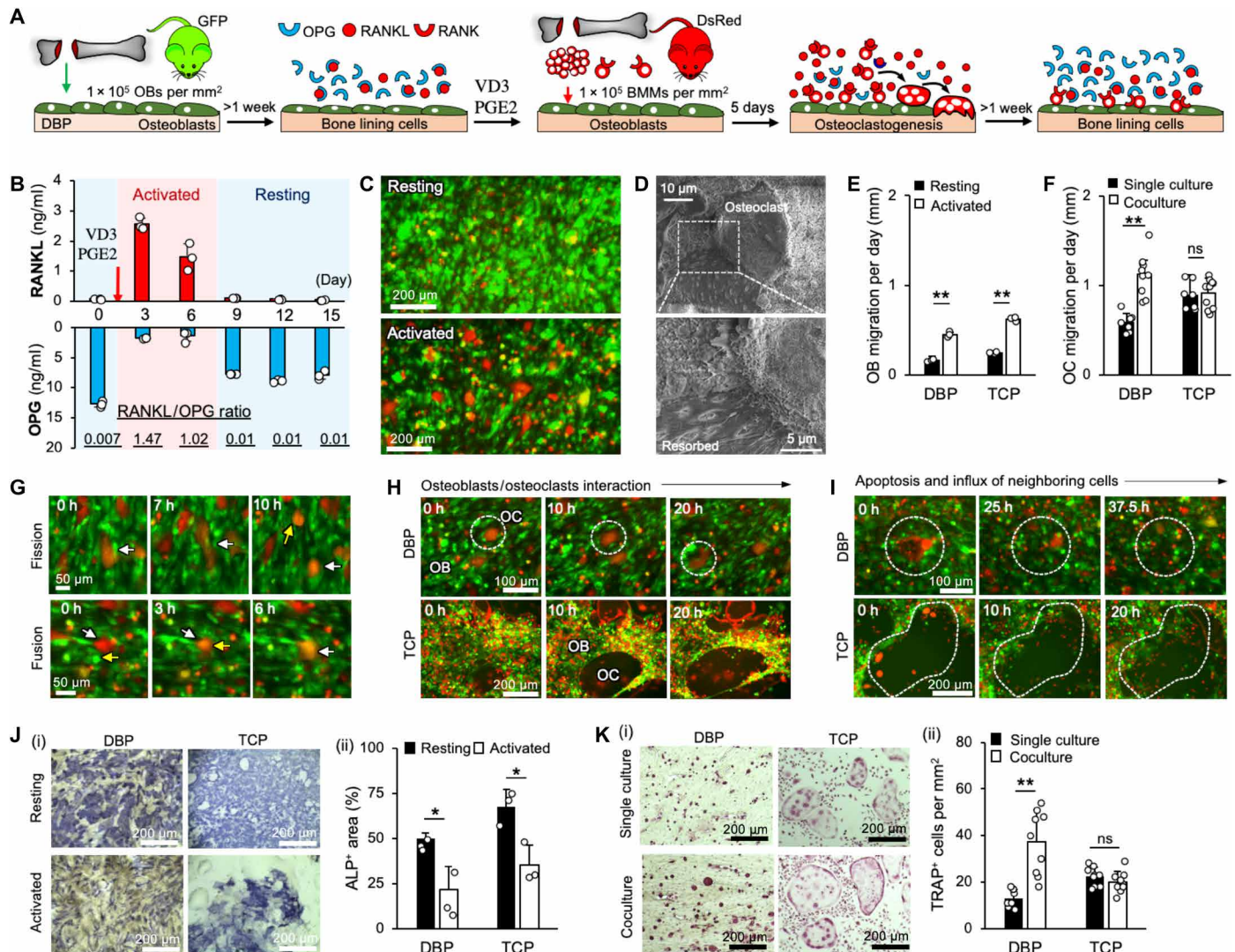
Fig. 4. The bone remodeling cycle is recapitulated by coculture of bone lining cells and BMMs on DBP under chemical stimulation. (**A**) Experimental procedure to simulate a bone remodeling cycle. (**B**) Stimulation of bone lining cells on DBP with VD3 and PGE2 caused a temporary increase in RANKL/OPG secretion ratio ($n = 3$ to 5). (**C**) Representative fluorescent images show that activated OBs (green) induce BMMs (red) to differentiate into osteoclasts (OCs). (**D**) SEM confirmed functional mineral resorption by OCs. (**E**) Stimulated OBs migrated two times faster than their unstimulated counterparts on both DBP and TCP ($n = 4$). (**F**) OC migration in single culture and coculture on DBP and TCP ($n = 10$). (**G**) On DBP, OCs underwent both cell fission and cell fusion. (**H**) On TCP, OBs were readily pushed by large multinucleated OCs, whereas on DBP, the OBs stayed in place. (**I**) On TCP, OCs underwent cell fusion repeatedly until cells became giant and underwent apoptosis. After apoptosis, the large actin-ring structure of the OC remained and prevented immediate migration of neighboring OBs. (**J**) (i) Alkaline phosphatase (ALP) staining of OBs and (ii) quantitative comparison ($n = 3$ to 6). (**K**) (i) Tartrate-resistant acid phosphatase (TRAP) staining of multinucleated OCs and (ii) quantitative comparison ($n = 10$) (*$P < 0.05$, **$P < 0.01$, ns, not significant).

Detailed time-lapse imaging captured cellular migration activity on both materials. Stimulated osteoblasts migrated two times faster than their unstimulated counterparts on both DBP and TCP (Fig. 4E). On DBP, osteoclasts cocultured with stimulated osteoblasts migrated twice as fast as osteoclasts stimulated in the absence of osteoblasts. On TCP, osteoclasts cocultured with stimulated osteoblasts migrated at the same rate as osteoclasts stimulated in the absence of osteoblasts (Fig. 4F). On DBP, osteoclasts underwent cell fusion and cell fission, in which individual cells separated from the multicellular body (Fig. 4G and movie S9) (*30*). By contrast, osteoclasts on TCP underwent cell fusion repeatedly until the cells became giant and multinucleated and cell death occurred by apoptosis. As a result of

the repeated cell fusion, the osteoclasts on TCP exhibited a broad range of cell sizes (720 ± 400 μm^2). Osteoclasts on DBP were significantly smaller and had narrower cell size distribution (140 ± 43 μm^2), similar to that seen in trabecular bone (*31*). Osteoclasts cultured on DBP and TCP had a similar ratio of number of nuclei to cell area (fig. S7). Active osteoblasts on DBP held their position in the presence of osteoclasts, whereas osteoblasts on TCP were pushed aside by migrating osteoclasts (Fig. 4H). When osteoclasts on TCP underwent apoptosis, they left behind large actin-ring structures that prevented migration of neighboring osteoblasts. Instead, BMMs were the first to migrate to the region that had been occupied by the dead cell body, because they are floating cells, and osteoblasts entered

10 hours later. A similar process occurred on DBP but was less pronounced because the osteoclasts were smaller and apoptosis was infrequent (Fig. 4I and movie S10).

Recent data suggest that osteoblasts promote osteoclast differentiation and osteoclasts enhance osteoblast activity (32). We examined the coupling of osteoblast and osteoclast activities by measuring changes in osteoblast- and osteoclast-specific functional enzyme activities under VD3 and PGE2 stimulation. We focused on alkaline phosphatase (ALP), which is expressed by osteoblasts during mineral deposition, and tartrate-resistant acid phosphatase (TRAP), which is expressed by osteoclasts during mineral resorption. Before stimulation, osteoblasts expressing ALP covered 50% of the surface of DBP and 67% of the surface of TCP; after stimulation, this was reduced by half on both substrates (Fig. 4J). This indicates that half of the bone lining cells actively deposit mineral and that activation interrupts the mineral deposition process. Nearly all multinucleated osteoclasts expressed TRAP. The number of TRAP+ osteoclasts on DBP increased threefold when the osteoclasts were cocultured with osteoblasts, whereas TRAP+ osteoclast numbers on TCP were not affected by coculture with osteoblasts (Fig. 4K). This result, along with the increased motility of osteoclasts on DBP (Fig. 4F), indicates that DBP effectively facilitates cross-talk between osteoblasts and osteoclasts. These results suggest that DBP faithfully reproduces the bone remodeling cycle and provides a quantitative analytical platform to probe the multicellular processes of trabecular bone remodeling.

DBP-based trabecular bone organoid model recapitulates localized bone remodeling in trabecular bone cavities

In healthy trabecular bone, remodeling activity is confined to local spots surrounded by resting surfaces. The active and resting surfaces maintain different profiles of stimulatory and suppressive secretions, which results in a unique spatiotemporal pattern of regulatory molecules (3). Unbalanced remodeling with excessive bone resorption decreases bone thickness and increases cavity diameter (Fig. 5A). We hypothesized that localized bone remodeling is maintained by integrated metabolic and morphological regulation. To test this hypothesis, we simulated coexisting active and resting bone surfaces by culturing DBP disks with resting-state bone lining cells with DBP inserts with active osteoblasts. We created DBP inserts by fastening 100-μm-thick circles of DBP between two concentric O-rings. We built ring-shaped spacers to separate the resting-state and active-state surfaces to simulate the space in trabecular bone cavities (Fig. 5B). We used 6-, 10-, and 14-mm-diameter inserts to represent different-sized areas of active bone surface, and we used 0.5-, 1.5-, and 4.5-mm spacers to simulate different-sized trabecular bone spaces. We added BMMs to the space between the DBP disk and the DBP insert. The BMMs undergo osteoclastogenesis in response to spatiotemporal gradients of regulatory molecules. The ability to systematically manipulate the relative area of active to resting surfaces and the distance between them allowed investigation of the role of spatiotemporal profiles of regulatory molecules in localized bone remodeling. We named this setup the trabecular bone organoid model (Fig. 5C).

We began our study by examining the secretion profiles of the DBP inserts. Osteoblasts cultured on various-sized DBP inserts for 1 week acquired the bone lining cell phenotype, with low RANKL and high OPG secretion (Fig. 5Di). We then stimulated the cells with VD3 and PGE2 (two times, 3 days apart, to ensure that all cells were activated) and observed that RANKL secretion increased in proportion to the size of the insert and OPG secretion decreased the same amount regardless of insert size (Fig. 5Dii). Next, we assembled the trabecular

bone organoid model by placing a 16-mm DBP disk with bone lining cells in the well of a 24-well plate, adding 1×10^6 BMMs, and placing the stimulated DBP insert in the well over a spacer. We replaced the activated DBP insert after 3 days to maintain the level of stimulatory molecule secretion and terminated the coculture by 6 days (Fig. 5E).

We applied this trabecular bone organoid model to study the effect of spatiotemporal profiles of stimulatory and suppressive molecules on the activation of bone lining cells and the differentiation of BMMs into osteoclasts under two distinct scenarios. First, we examined the effect of activated surface area by testing three sizes of DBP inserts with one spacer height (0.5 mm). At the end of 6 days of coculture, we quantified the activation of lining cells by measuring the ALP+ osteoblast area and quantified the differentiation of osteoclasts by counting the number of TRAP+ multinucleated cells. The results showed a stepwise increase in osteoclast number with increasing DBP insert size. ALP production of bone lining cells was significantly lower with the 14-mm insert than it was with the 10-mm insert (Fig. 5F). We then examined the impact of the gap (spacer) dimension by testing three spacer heights with one DBP insert size (14-mm diameter). After 6 days of coculture, we observed a stepwise decrease in osteoclast number with increasing spacer height. There was no significant difference in the ALP+ osteoblast area (Fig. 5G). These results indicate that BMMs and bone lining cells are both responsive to the extent and gradient of stimulative molecules, but differentiation of BMMs into osteoclasts occurs in a more localized pattern than activation of bone lining cells does.

Quantitative spatial mapping of cellular activities in the trabecular bone organoid model shows effect of spatiotemporal profiles of regulatory molecules on bone remodeling activity

We developed an algorithm for multiplex quantitative mapping of cellular bone remodeling activities to elucidate the effects of spatiotemporal profiles of regulatory molecules on BMMs and bone lining cells. First, we conducted full surface scans of a DBP disk with four fluorescent channels: GFP, to distinguish cells from DBP; 4′,6-diamidino-2-phenylindole (DAPI), to determine the number of nuclei in each cell; TRAP, to monitor osteoclast emergence; and ALP, to measure osteoblast activation (Fig. 6A and fig. S8). We averaged three independent results and generated spatial heatmaps of osteoblast and osteoclast activities relative to unstimulated controls (Fig. 6B). For statistical comparison, we discretized the surface of the DBP disk into seven concentric zones with 1-mm-radius increments and plotted average fold changes of osteoclast and osteoblast activities within each zone. We drew a trend line and determined the slope and regression that describes the functional connection between spatiotemporal gradients of stimulatory molecules and local bone remodeling activity. There was no significant difference in spatial distribution of fluorescent markers in the unstimulated controls (Fig. 6C).

We repeated multiplex quantitative imaging analysis for trabecular bone organoid models with three insert sizes and three spacer heights. We placed 6-, 10-, or 14-mm-diameter activated DBP inserts above DBP disks with bone lining cells, separated by a 0.5-mm-high spacer, in the well of a 24-well plate (Fig. 6D, i to iii). In wells with 6-mm inserts, the overall number of osteoclasts was no different from that of the unstimulated control, but spatial analysis revealed that the average fold change of osteoclasts in zones 1 and 2 was five times higher than it was in zones 3 through 7. Spatial analysis of
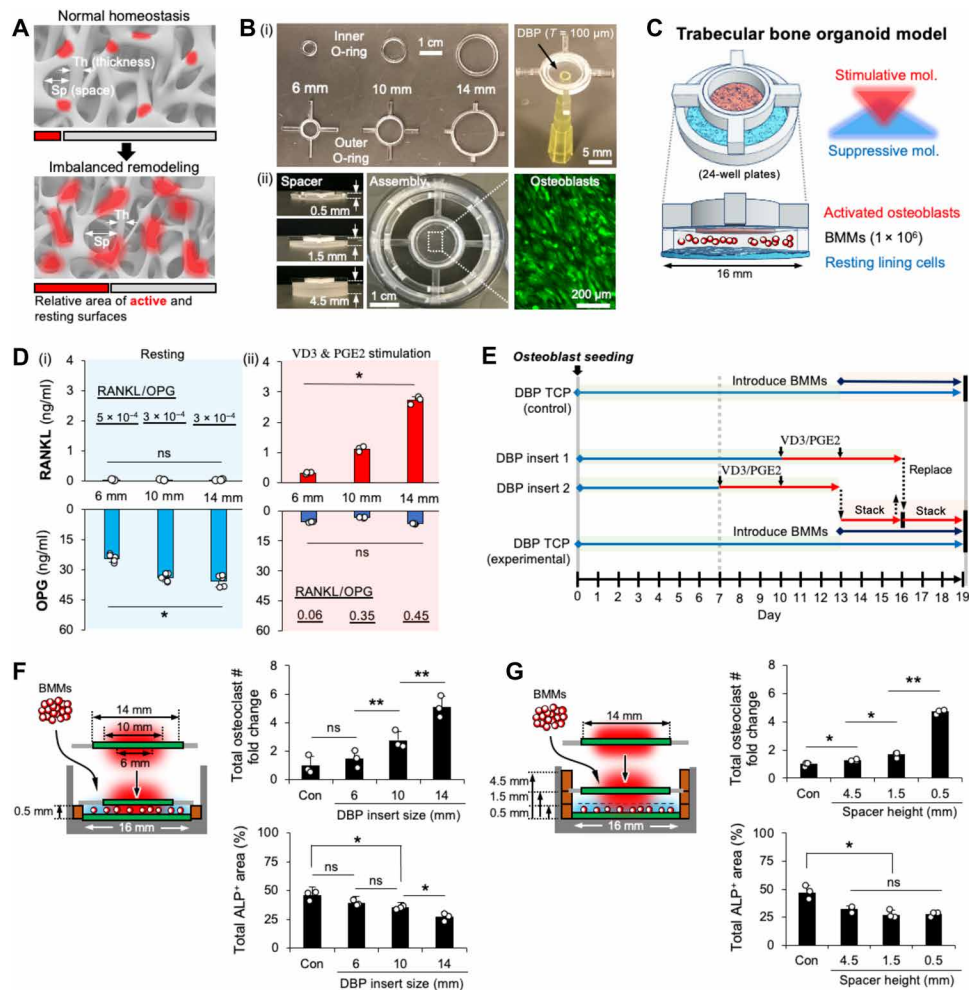
Fig. 5. The trabecular bone organoid model recapitulates coexisting active and resting bone surfaces. (**A**) Excessive bone remodeling results bone loss and changes in the trabecular bone morphology, which could compromise anatomical regulation of localized bone remodeling. (**B**) (i) DBP inserts were prepared by securing 100-μm-thick DBP between two acrylic O-rings. (ii) DBP inserts were suspended above DBP disks with ring-shaped spacers. OBs cultured on a DBP insert. (**C**) The trabecular bone organoid model consists of a DBP insert that has been activated by VD3 and PGE2 suspended over a DBP disk containing bone lining cells. This juxtaposition of active and resting surfaces with a shared microenvironment simulates in vivo–relevant gradients of stimulatory and suppressive molecules. (**D**) (i) OBs cultured on DBP inserts acquired the bone lining cell secretory profile. (ii) VD3 and PGE2 stimulation increased RANKL secretion in proportion to surface area of insert ($n = 5$). (**E**) Experimental design. (**F** and **G**) DBP with bone lining cells was cocultured with BMMs and (F) three insert sizes or (G) three spacer heights. After 6 days of coculture, TRAP⁺ multinucleated OCs and total area of ALP⁺ OBs were measured ($n = 3$) (*$P < 0.05$, **$P < 0.01$, ns, not significant). Photo credit: Yongkuk Park, University of Massachusetts Amherst.

10- and 14-mm DBP inserts revealed a stepwise increase in osteoclast number from the edge to the center of the DBP disk. Linear analysis of the correlation between osteoclastogenesis and distance from the center of the DBP disk showed that the slope values increased with insert diameter. The average regression value was 0.66 across all insert sizes. Next, we analyzed ALP expression change in the osteoblasts on the DBP disk. In wells with 6- and 10-mm DBP inserts, the overall percentage of ALP⁺ osteoblasts was not significantly different from that of the unstimulated control; however, spatial analysis revealed a 20% decrease in ALP⁺ osteoblasts in zones 1 and 2 in wells with a 6-mm DBP insert and a 17% decrease in ALP⁺ osteoblasts in zones 1 through 3 of wells with a 10-mm DBP insert. The slope value decreased as DBP insert diameter increased from 6 to 14 mm, and the average regression was 0.78. These results capture the effect of the size and distance of activated surfaces on localized activation of BMMs and bone lining cells.

We repeated the experiment with the 14-mm-diameter insert and three spacer heights: 0.5, 1.5, and 4.5 mm (Fig. 6D, iii to v). When the gap size increased, overall osteoclast differentiation decreased and localization to the central regions weakened. Slope values for osteoclast differentiation decreased as gap size increased. Regression analysis produced a value of 0.47 for the largest gap size, which indicates reduced impact of the activated surface on BMMs. When the gap size increased from 0.5 to 4.5 mm, the ALP expression slope values approached zero, which indicates poor correlation to a localized phenomenon. However, average ALP⁺ area did increase with increasing spacer height. These results indicate that localized activation of bone lining cells is sensitive to concentration of stimulative molecules but less dependent on distance of activated surfaces than differentiation of BMMs is. Osteoclastogenesis was affected by both active area and distance but had a stronger correlation with active area.
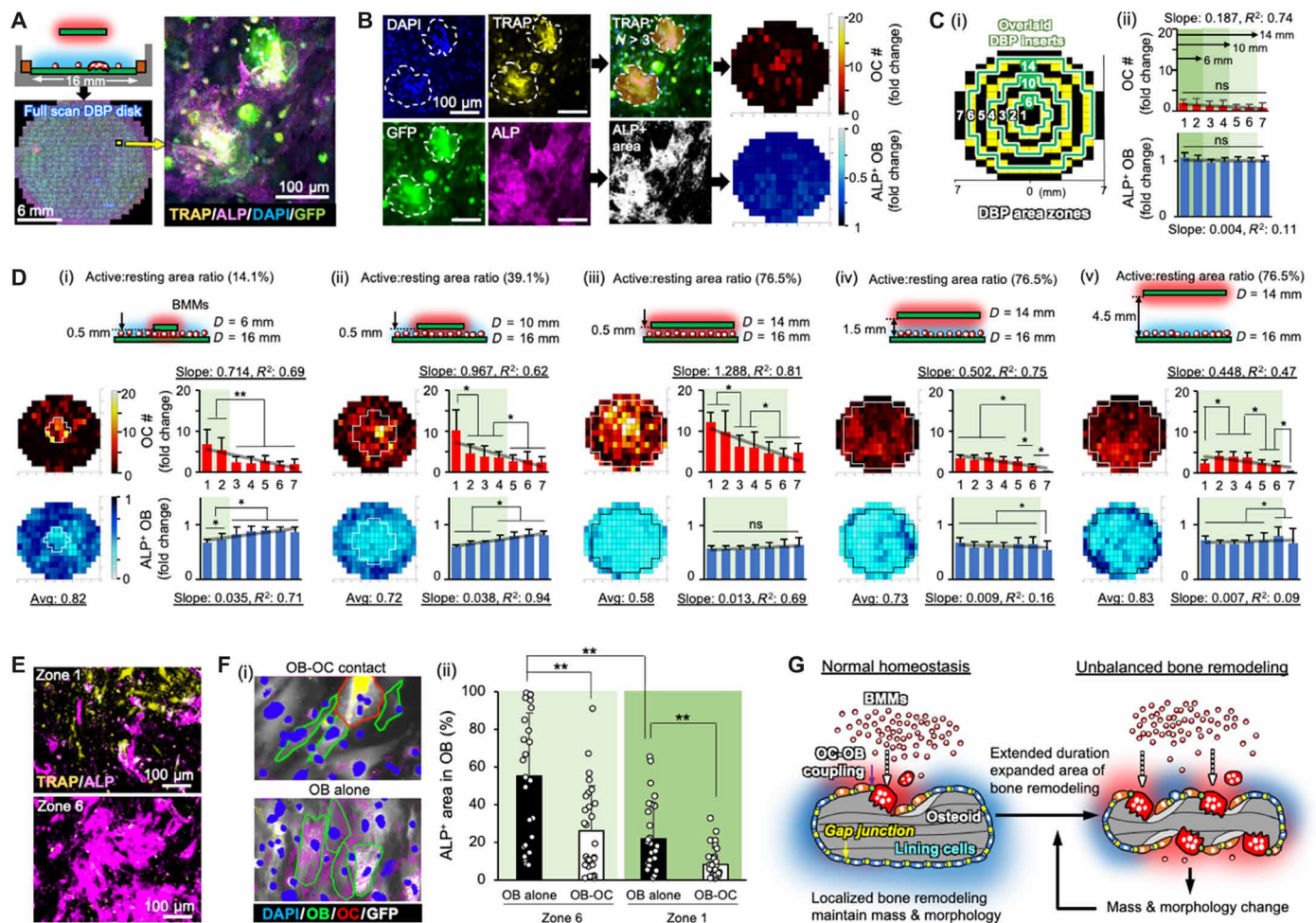
Fig. 6. Quantitative spatial mapping of OBs and OCs captures paracrine- and cellular contact–mediated regulation of bone remodeling. (**A**) DBP disks in a well plate were scanned with fluorescent channels for TRAP, ALP, GFP, and DAPI. The resulting 218 multiplex images were stitched together to represent the entire surface of the DBP disk. (**B**) Illustration of quantitative spatial imaging analysis for creating heatmaps of counts of TRAP+ and multinucleated (>3) OCs (top) and areas of ALP+ and GFP+ OBs (bottom). (**C**) (i) The DBP surface was discretized into seven concentric zones. (ii) Plot of activity levels for each region in control. (**D**) Representative heatmaps of ALP+ OB activity and regional OB and OC activities with linear analysis to correlate localized bone remodeling cellular activity and paracrine signaling from coculture experiments (n = 3 to 5). (**E**) Representative images of TRAP and ALP in central zone 1 and peripheral zone 6. (**F**) (i) Representative multiplex images showing delineation of OCs and OBs. (ii) Quantitative comparison of ALP+ OBs that are and are not in direct contact with OCs (n = 30). (**G**) Proposed mechanism of localized trabecular bone remodeling regulation (*P < 0.05, **P < 0.01, ns, not significant).

Functional coupling of osteoblasts and osteoclasts can occur by means of direct contact and by paracrine signaling (*33*). Therefore, we examined whether localized bone remodeling activity is affected by direct contact between osteoblasts and osteoclasts. The central zone of the DBP disk accommodates higher numbers of osteoblasts and osteoclasts than the peripheral zones. To distinguish between the effect of stimulatory molecules and the effect of physical contact between osteoclasts and osteoblasts, we repeated the experiment with 6-mm DBP inserts. We measured the reduction of ALP in individual osteoblasts that were not in contact with osteoclasts in zone 1, which was exposed to high levels of stimulatory molecules, and in zone 6, which was exposed to low levels of stimulatory molecules (Fig. 6E and fig. S9). In zone 6, 55% of osteoblasts that were not in contact with osteoclasts were expressing ALP, whereas in zone 1, 22% of osteoblasts that did not have contact with osteoclasts were expressing ALP. This indicates that localized paracrine signaling activated

bone lining cells. In both zones, osteoblasts that were in contact with osteoclasts were half as likely to express ALP as osteoblasts that were not in contact with osteoclasts. This indicates that osteoclasts activate bone lining cells via direct contact. These results suggest that there is a synergetic effect between localized stimulative paracrine signaling and osteoblast-osteoclast contact in the regulation of bone remodeling (Fig. 6F). Collectively, studies with the trabecular bone organoid model show the importance of spatiotemporal profiles of regulatory molecules and direct contact between osteoblasts and osteoclasts in regulating local trabecular bone remodeling.

DISCUSSION
To effectively reproduce the bone remodeling cycle, an in vitro bone tissue model should (i) be built from bone-relevant biomaterials that support intrinsic phenotypes and processes of osteoblasts and

osteoclasts, (ii) include bone lining cells to simulate activation and termination of bone remodeling, and (iii) coculture osteogenic and hematopoietic cells to reproduce their functional interactions in the regulation of bone metabolism. With this in mind, we developed a tissue-engineered trabecular bone organoid model to investigate spatiotemporal aspects of molecular and cellular regulation of bone remodeling.

The trabecular bone organoid model is based on DBP, a bone-derived biomaterial that supports intrinsic phenotypes and processes of osteoblasts and osteoclasts—cells that exclusively reside and function on the bone surface. DBP serves as a functional template on which osteoblasts rapidly deposit structural minerals, guided by the lamellar structure of the dense collagen, and resultantly form osteoid bone having a depth similar to that seen in vivo (34). DBP's semitransparency makes it possible to monitor ongoing cellular processes with fluorescent microscopy, and it is thin but durable enough to be handled easily. The consistent thickness and diameter of DBP support reproducible functional assays including osteoclast mineral resorption, bone surface healing, and osteoblast metabolic switching assays. DBP can be produced in large quantities—more than 5000 from one bovine femur—for high-throughput and high-content experiments. The model's modular design allows it to be integrated with other models to represent additional tissue complexity. For example, the space between two DBPs could be filled with marrow-mimicking viscous gels (35, 36), porous scaffolds (37, 38), or microfluidic chips (39, 40).

Bone lining cells cover most of the trabecular bone surface and likely play a significant role in biochemical regulation (27), but they are difficult to study because we do not currently have definitive surface markers to distinguish bone lining cells from osteoblasts. DBP addresses this limitation by facilitating functional investigation of the bone lining cell phenotype. Our experiments captured phenotypic distinctions between bone lining cells and osteoblasts on TCP and DBP including morphology, migration, proliferation, and secretion (fig. S10). Osteoblasts on DBP rapidly take on the bone lining cell phenotype, confirmed by the appearance of organized cellular morphology with gap junction communication, lower migration and proliferation, higher OPG secretion, and lower RANKL secretion than osteoblasts on TCP. The bone lining cells on DBP demonstrated the ability to regain osteoblast activity when they were replated on TCP in the phenotypic switching assay, physically disrupted in the bone surface healing assay, or chemically stimulated with VD3 and PGE2. These results are consistent with recent in vivo findings that bone lining cells are a major source of osteoblasts (29). Under chemical stimulation, the bone lining cells switched from a suppressive secretory profile (high OPG and low RANKL) to a stimulatory secretory profile (low OPG and high RANKL). This suggests that bone lining cells use paracrine signaling to actively regulate the extent and duration of localized bone remodeling. To the best of our knowledge, this is the first demonstration of a bone remodeling cycle that includes the controlled and reversible activation of bone lining cells under physiologically relevant chemical stimulation. This makes it possible to study the initiation and termination of bone remodeling, which is difficult to do with existing models.

We simulated the coexistence of active and resting bone tissue surfaces by placing DBP disks with bone lining cells and BMMs in multiwell plates with DBP inserts containing stimulated osteoblasts. This setup enabled us to integrate osteogenic and hematopoietic cells in the context of trabecular bone cavities. The combination of resting and active DBP surfaces created defined spatiotemporal profiles of regulatory molecules, and BMMs introduced into the gap responded to the regionally concentrated paracrine signaling. The effect of the gap size between the DBP disk and the insert was weak, possibly because the selected gap dimensions were too large to capture the gradient effect (13). The area of the activated DBP insert correlated positively with differentiation of BMMs into osteoclasts and activation of bone lining cells. Multiplex quantitative spatial analysis captured differences between BMMs and bone lining cells in the spatial pattern of response to paracrine molecules. These differences could be due to differences in cellular organization between osteogenic and hematopoietic cells (41). Osteogenic cells develop multicellular organization and gap junction communication and thus respond to stimuli as a collective group (28). This collective response could attenuate their responsiveness to the gradient of stimulant signals and result in weak responsiveness. On the other hand, hematopoietic cells reside and function individually in the bone marrow (41), which could cause them to be more sensitive to gradients of stimulative molecules and have a stronger spatial pattern of responsiveness. Our results suggest that trabecular bone thickness and the number of osteogenic cells and their connectivity may be critical to keep bone remodeling localized. Quantitative image analysis elucidated the functional coupling between osteoblasts and osteoclasts. Coculture with osteoblasts increased differentiation and migration of osteoclasts. ALP expression in osteoblasts appeared to decrease as a result of direct contact with osteoclasts. Interactions between osteoblasts and osteoclasts have been viewed as individual cellular interactions (42), but our results suggest that individual hematopoietic cells interact with groups of osteogenic cells. Along with metabolic and anatomical considerations, this may be another intrinsic regulatory mechanism that confines localized bone remodeling activity (Fig. 6G).

The trabecular bone organoid model has a number of limitations. (i) Like all in vitro models, the media composition in the trabecular bone organoid model has higher concentrations of growth factors and stimulants than that seen in the body. (ii) Although the model induces relevant osteogenic cell types and demonstrates functional bone remodeling activities, the quantities and maturation stages of cells may not reflect actual physiology. (iii) The model does not include osteocytes, which comprise more than 95% of bone cells (43). Emerging evidence indicates that osteocytes actively regulate bone surface remodeling by secreting OPG, RANKL, and sclerostin (43–45). (iv) Mechanical aspects of trabecular bone regulation are absent. Trabecular bone is under constant mechanical stress and undergoes repeated microfractures, which play an important role in initiating localized bone remodeling (46). (v) The role of hematopoietic cells in regulating bone remodeling is not fully addressed. One study reported that more than 40% of bone marrow OPG is derived from B cells (47). In addition, allogeneic hematopoietic stem cell transplantation often accelerates osteoporotic bone loss (48), which suggests that hematopoietic cells can trigger imbalance in the microenvironment of the trabecular bone. (vi) The model does not adequately account for the inflammatory response. Trabecular bone contains bone marrow stromal cells that secrete various immunomodulatory molecules (49), and their profile is an important determinant of bone metabolism. We expect that incorporating these aspects of bone and marrow tissue complexity will allow the model to better capture the complex and dynamic biological processes of the bone-marrow interface.

In future work, the trabecular bone organoid model could be humanized for translational research by replacing bovine bones and

mouse cells with human bones and cells. The humanized trabecular bone organoid model could improve the predictive power of preclinical studies and shorten the screening period for osteoporosis drugs, which currently takes 6 to 14 weeks in preclinical animal studies and 12 to 24 months in clinical trials (*50*). The model could also help researchers determine drugs' mechanism of action and could be used to study the role of bone metabolism in hematopoietic stem cell regulation and dormant disseminated tumor cell biology. Future studies could directly compare the biological relevance and significance of the trabecular bone organoid model with existing biomaterial platforms for functional osteogenic cell assays such as bone slices and hydroxyapatite-coated plates. We envision that this in vitro trabecular bone organoid model will facilitate the study of numerous aspects of bone biology in health and disease.

MATERIALS AND METHODS

All chemicals and materials were purchased from Sigma-Aldrich or Thermo Fisher Scientific unless specified. All animal procedures were approved by the Institutional Animal Care and Use Committee of the University of Massachusetts Amherst. Experiments with and handling of mice were conducted in accordance with federal, state, and local guidelines.

Preparation of demineralized compact bovine bone blocks

Bovine femurs were obtained from a local slaughterhouse and cut into chunks. Bone marrow was removed by centrifugation, and muscle tissues were removed with a scalpel. The chunks were then cut into smaller pieces and treated with a 1:1 chloroform-methanol solution to dissolve residual lipids and cell debris. The cleaned bone pieces were submerged in 400 ml of 1.2 N hydrochloric acid (HCl) solution to remove minerals from the bone matrix. Under atmospheric pressure, the demineralization process of bovine compact bone (~1-cm thick) took more than 3 months with multiple rounds of HCl solution changes. To accelerate demineralization, we manufactured a programmable cyclic pressure chamber that consisted of an air-tight stainless-steel chamber (1 liter) and a solenoid valve programmed for various on/off intervals by an Arduino controller. Two to three cleaned bone pieces were submerged in HCl solution (200 ml) in a glass beaker that was then placed in the pressure chamber. The chamber was pressurized (≤4 bar) with in-house compressed air, which was then released after a programmed delay. After a first round of 24 hours of on/off pressure cycle operation, the demineralized outer layer of bone and a periosteal fibrous film were removed with a razor blade to ensure full exposure of the bone matrix. Incomplete removal of a periosteal fibrous film causes inefficient and inconsistent demineralization. A second round of cyclic hydrostatic pressure was applied for 48 hours, the HCl solution was replaced, and the bone pieces were treated with another 48 hours of cyclic hydrostatic pressure. Last, the demineralized bone pieces were stabilized in deionized (DI) water overnight. To determine the depth of demineralization, the processed bone pieces were soaked in rhodamine dye solution for 10 min and then cut into two pieces. The cross-sectional images were analyzed with ImageJ to determine the depth of dye penetration. Optimal pressure and on/off cycles were determined by orthogonally changing the pressure (1, 2, 3, and 4 bar) and on/off interval (10 s and 1, 5, and 10 min). The established protocol of 4 bar and 10-s on/off interval demineralized 1-cm thickness of compact bone piece within 1 week.

Radiographic imaging of demineralized bone blocks

Complete removal of mineral after the demineralization process was confirmed by radiographic imaging (Faxitron MX-20 X-ray cabinet) at 1 mA, 34 KV. Brightness of radiographs was quantitatively measured by ImageJ.

Preparation of DBP

Demineralized bone pieces were embedded in optimal cutting temperature medium, frozen at −20°C, and sliced into thin sections with a cryostat (CryoStar NX70). Thickness of slices was adjustable within the range of 10 to 150 μm; the 20-μm thickness was used in this study. The sectioned demineralized bone matrix was soaked in 8% sodium dodecyl sulfate solution overnight to remove remaining cell debris. Decellularization was confirmed by significantly reduced nuclear DAPI staining. Decellularized bone slices were then washed with DI water three times and stored in 70% ethanol at 4°C. At this stage, the biomaterial is referred to as DBP. More than 5000 quality DBPs were produced from one bovine femur. DBPs were cut with biopsy punches into circular shapes to be placed in multiwell plates; 6-, 10-, 14-, and 16-mm-diameter DBPs were prepared for 96-, 48-, 24-, and 12-well plates, respectively. Before use, DBPs were sterilized with 70% ethanol for 15 min and then washed with phosphate-buffered saline (PBS) three times with 10-min intervals.

Characterization of DBP
Mechanical properties

Different thicknesses of DBP (20, 50, and 100 μm) were cut into dog-bone shapes and gripped in a mechanical testing machine (ElectroForce 5500, TA Instruments). The DBP was stretched at a rate of 0.4 mm/s at room temperature, while applied tensile force and displacement of grips were continuously measured with XEI software (TA Instruments) until failure. A stress-strain curve was plotted in Excel from which Young's moduli were determined.
Optical transparency

To quantify absorbance, a circular hole (20-mm diameter) was made at the center of the plastic bottom of a six-well plate with a laser cutting machine (Epilog Laser). DBPs of various thicknesses (20, 50, and 100 μm) were placed over the hole, and a cover-glass slide was used as a control. The absorbance of DBPs and the glass slide was measured at a wavelength of 600 nm by a microplate reader (Synergy 2, BioTek). Relative optical transparency was determined by setting the cover-glass slide absorbance as 100%.
Surface morphology

Surface morphology of DBPs was observed optically under a tissue culture microscope. DBPs were dried and coated with gold by a sputter coating machine (CR108, Cressington) and imaged with SEM (FEI Magellan) for detailed characterization of surface morphology.
Biochemical intactness of collagen fibers

CHP conjugated with fluorescein isothiocyanate was provided by M. Yu (University of Utah). For a positive control, damaged collagen matrix was prepared by submerging DBP in an 80°C water bath. Before use, a CHP stock solution was incubated in the water bath at 80°C for 5 min to dissociate coiled trimeric strands into monomeric strands. The heated solution was cooled on ice for 30 s. Intact and damaged DBPs were incubated overnight in 10 μm of CHP solution at 4°C. The CHP bound on damaged collagen fibers was imaged under a fluorescence microscope (EVOS).

Retrieval and expansion of murine osteogenic cells

DsRed mice were obtained from B. Osborne (UMass Amherst), and GFP mice were obtained from The Jackson Laboratory (003291). Mice aged 6 to 12 weeks were used for the study. Femurs and tibias were harvested intact, and the surrounding connective tissues were removed. After the epiphyses were removed, the open-ended long bones were placed in 0.5-ml microcentrifuge tubes with holes punched in the bottom with a 26-gauge needle, and those tubes were inserted in 1.5-ml microcentrifuge tubes with the cap closed. During centrifugation at 10,000g for 30 s, the entire bone marrow was released into the 1.5-ml tubes. The marrow-emptied long bones were gently cut into 1- to 2-mm lengths with a scalpel. These bone chips were placed in a T25 flask with 3 ml of digesting medium composed of α-minimum essential medium (α-MEM), 1% penicillin-streptomycin (PS), and 800 U of collagenase. After 1 hour of incubation at 37°C, the digesting medium was replaced with expansion medium composed of α-MEM supplemented with 1% PS and 10% fetal bovine serum (FBS). Osteogenic cells migrated out from bone chips and proliferated on TCP. Once 80% confluency was achieved, the cells were detached with 1% trypsin/EDTA and subcultured in T175 flasks for further expansion. Cells were cultured at 37°C in a humidified atmosphere containing 5% CO_2. Cells used for experiments were subcultured less than five times.

Osteoblast differentiation

Expanded osteogenic cells were cultured in osteoblast differentiation medium composed of α-MEM supplemented with 1% PS, 10% FBS, 10 mM β-glycerophosphate, and 200 μM L-ascorbic acid.

Osteoblast functional assays
Osteogenic cell morphology and alignment

The osteoblasts were cultured for 1 week in osteogenic differentiation medium and fixed with 4% paraformaldehyde. Cytoskeletal actin filaments and nuclei were stained with phalloidin conjugated with Alexa Fluor 488 and DAPI, respectively. Confocal microscopy (Zeiss Cell Observer SD) was used for imaging. Cell alignment angles were measured with the angle tool function of ImageJ. Cell alignment angles on TCP and DBP were measured with respect to the horizontal line and the average of collagen alignment of DBP, respectively. The 0° angle was set on the basis of collagen alignment angle of DBP. A total of 100 measurements from 10 different samples were used to generate a circular diagram that was produced in MATLAB.

Osteogenic migration under long-term fluorescent time-lapse imaging

Endogenous GFP and DsRed fluorescence of osteogenic cells was detected with an inverted fluorescent microscope with a 10× objective lens (LumaScope 720, Etaluma) that operates inside of a CO_2 incubator. Quantitative cell migration analysis was conducted by processing obtained images using TrackMate in ImageJ. Time-lapse movies were prepared with ImageJ.

Collagen deposition and alignment

A resonant scanning multiphoton microscope (Nikon A1MP) was used to image collagen fibers deposited by osteoblasts via second harmonic generation with a 25× objective lens. Collagen fibers were excited at 810 nm. Alignment angles of individual collagen fibers were measured with the angle tool function of ImageJ. Collagen alignment angle on TCP and DBP was measured with respect to the horizontal line on TCP and the average of collagen alignment on

DBP. A total of 100 measurements from 10 different samples were used to generate a circular diagram.

Mineral deposition

Mature osteoblasts were cultured on TCP and DBP for up to 3 weeks with osteogenic differentiation medium. At the end of the experiment, cells were fixed with 4% formaldehyde for 5 min, washed three times with DI water, and stained.

Alizarin red mineral staining. Fixed samples were stained with alizarin red (American MasterTech) for 30 min and washed with DI water until the washing solution appeared clear. Mineral stained with alizarin red was imaged with an optical microscope (EVOS) with a 10× objective lens. Deposited mineral was quantified by solubilizing alizarin red in 10% acetic acid for 1 hour and measuring the absorbance of the solution at 405 nm with a microplate reader (BioTek).

Fluorochrome calcein mineral staining. Because calcein emits green fluorescence, osteogenic cells were derived from DsRed mice. Fixed samples were stained with 50 μM calcein solution. The fluorescence of calcein and DsRed osteogenic cells was imaged under confocal microscopy with 10× and 20× objective lenses.

Chemical remineralization of DBP in SBF. To prepare 1 liter of 10× SBF solution, 58.43 g (1 M) of NaCl, 0.373 g (5 mM) of KCl, 3.675 g (25 mM) of $CaCl_2·2H_2O$, and 1.016 g (5 mM) of $MgCl_2·6H_2O$ were dissolved in 600 ml of DI water (solution 1). In a separate glass beaker, 0.42 g (10 mM) of Na_2HPO_4 was dissolved in 30 ml of DI water (solution 2). Solution 2 and HCl were added to solution 1 dropwise to maintain pH below 4 to avoid calcium precipitation. DI water was also added to bring the final volume up to 1 liter while maintaining a pH of 4. For calcium precipitation, a small amount of $NaHCO_3$ was added in the 10× SBF solution to increase pH. For remineralization, DBP was submerged in the 10× SBF solution immediately after adding $NaHCO_3$ and incubated at 37°C for 5 hours.

Surface characterization

Imaging surface morphology. SEM was used to obtain high-resolution surface morphology of DBP, osteogenic cells, and deposited minerals. Osteogenic cells were fixed with 2.5% glutaraldehyde and rinsed with DI water. The fixed cells were dehydrated in sequential graded ethanol solution (50, 70, 80, 90, 95, and 100%) for 10 min each. The cells were dried at room temperature with hexamethyldisilazane. Before imaging, samples were coated with gold with a sputter coating machine.

Measuring surface roughness. Remineralized DBPs were heated at 500°C for 5 hours to thermally decompose the organic components. The remaining mineral layers were analyzed by an optical profiler (Nexview, Zygo) that visualized 3D surface morphology and quantitatively presented surface roughness.

Characterization of bone lining cells

DBP was seeded with $1 × 10^6$ osteoblasts/mm^2. After 1 week of culture with differentiation medium, osteoblasts fully covered the surface and exhibited the bone lining cell phenotype as characterized by the following methods.

Immunofluorescent staining of Ki67

Osteoblasts were fixed with 4% paraformaldehyde for 5 min at room temperature and washed three times with PBS. The fixed cells were incubated in PBS containing 0.1% Triton X-100 for 10 min and washed three times with PBS. For blocking, the cells were incubated with 10% goat serum and 1% bovine serum albumin (BSA) in PBS for 2 hours at room temperature. A primary rabbit anti-mouse Ki67 antibody (1:200 dilution in the blocking solution) was applied to the sample and incubated overnight at 4°C. After three washes with PBS,

a secondary goat anti-rabbit antibody conjugated with Alexa Fluor 647 (1:200 dilution in the blocking solution) was applied and incubated for 1 hour at room temperature. After three washes with PBS, a DAPI solution (100 μl of 10 ng/μl) was added before imaging. Images were obtained with fluorescence and confocal microscopy.

Bone surface healing assay
The cell surface was scraped with a sterilized acrylic rod (0.5-mm diameter). Time-lapse fluorescent imaging of the scratched area was conducted for 72 hours at 30-min intervals (LumaScope 720) in a CO_2 incubator. Recovery of the scratched area by awakened bone lining cells was quantified with ImageJ. Transiently increased osteogenic cell migration rates were measured with TrackMate in ImageJ.

Osteoblast phenotypic switching assay
Osteoblasts cultured on DBP with differentiation medium acquired a bone lining cell phenotype and reached full confluence after 2 weeks. The DBP with confluent bone lining cells was transferred to a T25 flask, and 3 ml of α-MEM with 800 U of collagenase II was added. After 1 hour of incubation at 37°C, the degraded DBP left behind mineralized fragments. The collagenase solution was carefully removed, and 5 ml of expansion medium was added. Osteogenic cells migrated out of the mineralized parts and culture-expanded on TCP. Expanded osteoblasts on TCP were detached with trypsin and EDTA and reintroduced on DBP to reinduce the bone lining cell phenotype, which is considered one cycle of this osteoblast phenotypic switching assay. In each cycle, the time to reach 80% confluency on TCP and the amount of mineral deposited in the 2-week culture on DBP were determined. We repeated three cycles of this phenotypic switching assay.

Characterization of gap junction communication among osteogenic cells on DBP
Immunofluorescent staining of connexin 43
Osteoblasts on DBP were fixed with 4% paraformaldehyde for 5 min at room temperature. The cells were then washed three times with PBS. Washed cells were incubated for 10 min with PBS containing 0.1% Triton X-100 and then washed three times with PBS. For the blocking step, the cells were incubated with 10% goat serum and 1% BSA in PBS for 2 hours at room temperature. Primary and secondary antibodies were diluted 1:50 and 1:200 in blocking solution, respectively. The cells were incubated overnight with rabbit anti-mouse connexin 43 antibody at 4°C. After washing three times with PBS, goat anti-rabbit antibodies with Alexa Fluor 647 were added to samples and incubated for 1 hour at room temperature. After washing with PBS three times, phalloidin conjugated with Alexa Fluor 488 and DAPI (100 μl of 10 ng/μl) was added. Fluorescence imaging was conducted with a confocal microscope.

Time-lapse fluorescence imaging of Ca^{2+} influx
For gap junction–mediated Ca^{2+} imaging, osteoblasts on DBP were incubated in calcium-free PBS for 5 hours and then loaded with 5 μM Fluo-4 AM in calcium-free PBS. After 1-hour incubation, the osteoblasts were washed with calcium-free PBS three times. Time-lapse fluorescent imaging of Ca^{2+} influx under potassium stimulation was performed with a confocal microscope with a 20× objective lens at 0.5 s per frame for 5 min (Cell Observer SD). The average pixel intensity of fluorescence in each individual cell was quantified with ImageJ.

Isolation of murine BMMs
Femoral and tibial bones were harvested, and the bone marrow was isolated as mentioned above. On average, more than 2×10^7 bone marrow cells were harvested from each mouse. Isolated whole bone marrow cells were plated on TCP with expansion medium supplemented with macrophage colony-stimulating factor (M-CSF; 20 ng/ml). After 3 days of culture, floating BMMs were separated from adherent stromal cells for osteoclast differentiation experiments.

Osteoclast differentiation
BMMs were seeded on TCP, remineralized decellularized DBP, and DBP with osteoblasts with osteoclast differentiation medium composed of α-MEM supplemented with 10% FBS, 1% PS, RANKL (40 ng/ml), and M-CSF (20 ng/ml). Osteoclast differentiation medium was replaced every 3 days.

Osteoclast characterization and functional assays
Osteoclast morphology and size
BMMs cultured in osteoclast differentiation medium were fixed with 4% paraformaldehyde. Actin filaments and nuclei were stained with phalloidin conjugated with Alexa Fluor 488 and DAPI, respectively. Confocal microscopy (Cell Observer SD) was used to visualize osteoclast-specific actin-ring structure with a nucleus. The number of nuclei in a single osteoclast was counted manually in ImageJ, and cells with more than three nuclei were considered to be mature osteoclasts. The size of an osteoclast cell body was calculated from the average vertical and horizontal diameters.

Osteoclast migration under long-term fluorescent time-lapse imaging
Endogenous GFP or DsRed fluorescence of BMMs was detected with a 10× objective lens (LumaScope 720). The resulting images were analyzed with TrackMate in ImageJ to quantify cell migration, and time-lapse movies were prepared in ImageJ.

Osteoclast mineral resorption confirmed by SEM
Scanning electron microscopy (FEI Magellan 400) was used to confirm mineral resorption by osteoclasts. Osteoclasts emerged after 7 to 10 days of culture in osteoclast differentiation medium and were fixed with 2.5% glutaraldehyde and rinsed with DI water. The cells were then dehydrated in ethanol and dried at room temperature with hexamethyldisilazane. Before SEM imaging, samples were coated with gold.

Osteoblast and osteoclast coculture experiments
Osteogenic cells retrieved from GFP mice were cultured on DBP in a 48-well plate with osteoblast differentiation medium for 1 week to induce a mature bone lining cell phenotype. Then, 1×10^6 BMMs retrieved from DsRed mice were introduced into the wells in stimulation medium composed of α-MEM, 10% FBS, 1% PS, PGE2 (1 μM), and VD3 (10 nM).

Functional characterization of osteoblast and osteoclast coculture
Determining OPG and RANKL secretion by enzyme-linked immunosorbent assay
OPG and RANKL proteins produced by osteoblasts were measured in conditioned media with an enzyme-linked immunosorbent assay (ELISA) kit (R&D Systems). Media samples were taken over the culture period and diluted 1:5 in reagent diluent to bring OPG and RANKL concentrations within the detection range of the assay. The assay was performed according to the manufacturer's instructions.

Time-lapse fluorescent imaging of the coculture and quantitative imaging analysis
GFP osteoblasts and DsRed-osteoclast precursor cells were cultured together in stimulation media. These cells were observed through a

10× objective lens with a fluorescence microscope (LumaScope 720) operated in a CO_2 incubator. Time-lapse movies were prepared in ImageJ.

TRAP activity
Cells were fixed in 4% formaldehyde and washed three times with DI water. Osteoclast differentiation was evaluated with a TRAP detection kit (387A, Sigma-Aldrich) according to the vendor's protocol. Stained cells were observed with an optical microscope.

ALP activity
Cells were fixed with 4% paraformaldehyde for 5 min and then washed with DI water three times. ALP detection kits (86C, Sigma-Aldrich) were used to analyze the ALP activity of osteoblasts. The staining was performed according to the vendor's protocol. Stained cells were observed with an optical microscope.

Preparation of DBP inserts
Inner and outer 0-rings were fabricated to interlock around DBP disks. The rings were designed in Adobe Illustrator and cut with a laser cutting machine from 1-mm-thick acrylic plates. The outer 0-rings were slightly larger than the DBP circles and had four side-bars to center the DBP insert in the well. The diameters of the inner O-rings were 6, 10, and 14 mm. Ring-shaped spacers were cut from acrylic plates with 0.5-, 1.5-, and 4.5-mm thicknesses. Fabricated O-ring inserts and spacers were sterilized with 70% ethanol before use in cell culture. Sterilized DBP rings were washed with PBS three times and placed in a 24-well plate before cell seeding.

Experimental setup for trabecular bone organoid model with a DBP insert
For the resting state, 1.5×10^5 osteoblasts were seeded on DBP (16-mm diameter) in a 24-well plate and cultured with differentiation medium for more than 1 week. For the activated state, 1.5×10^5, 7×10^4, and 2×10^4 osteoprogenitor cells were first seeded on 15-, 12-, and 8-mm-diameter DBP circles, respectively. The osteoblast seeded DBPs were gripped by the two concentrically assembled O-rings and cultured more than 7 days with differentiation medium. Bone lining cells on DBP inserts were stimulated with VD3 and PGE2 for two rounds of 3 days each. Next, 1×10^6 BMMs were added to each well. Stimulated DBP inserts were transferred to the 24-well plates with the osteoblasts facing the bottom of the plate. The distance between the resting and activated DBP surfaces was controlled with 0.5-, 1.5-, and 4.5-mm thick, ring-shaped spacers. During co-culture, the activated DBP insert was replaced with a newly activated DBP insert every 3 days to maintain the profile of secretory molecules from activated osteoblasts. Multiplex immunofluorescent staining was performed after 6 days of coculture.

Multiplex immunofluorescent staining and imaging
Osteoblasts and BMMs retrieved from GFP mice were used to perform multiplex imaging. After osteoblasts and osteoclasts were co-cultured in the trabecular bone organoid model, cells on DBPs in the 24-well plate bottom were fixed in 4% paraformaldehyde for 5 min at room temperature and washed three times with PBS. The fixed cells were incubated for 10 min with PBS containing 0.1% Triton X-100 and washed with PBS three times. The samples were blocked with 10% donkey serum and 1% BSA in PBS for 2 hours at room temperature. Primary goat anti-mouse ALP and rabbit anti-mouse TRAP antibodies were diluted 1:200 in blocking solution and added on the samples. After overnight incubation at 4°C, the cells were washed three times with PBS. Secondary donkey anti-goat antibodies conjugated with Alexa Fluor 568 and donkey anti-rabbit secondary antibodies conjugated with Alexa Fluor 647 were diluted 1:200 in blocking solution and added to samples. After 1-hour incubation at room temperature, the cells were washed with PBS three times. Before imaging, DAPI solution was added (200 μl of 10 ng/μl). The entire surface of multiplex imaging samples was scanned with fluorescence and confocal microscopes with 10× objective lenses.

Quantitative image analysis algorithm of multiplex immunofluorescent images
TRAP$^+$ multinucleated osteoclast number and ALP$^+$ osteoblast areas on DBP placed in a 24-well plate were quantified from multiplex immunofluorescent images with CellProfiler. Automatic quantification was validated by comparing the results against manually obtained data. For total analysis, osteoclast number and ALP$^+$ osteoblast area were averaged from three independent experiments. Fold change of osteoclast number and percentage of ALP$^+$ osteoblast area were calculated on the basis of the results from unstimulated control. For regional analysis, the bottom DBP was discretized into seven concentric regions in which TRAP$^+$ osteoclast number and ALP$^+$ osteoblast area were calculated. Fold change was determined by comparing the results of matching control experiment. For the characterization of ALP reduction of osteoblasts in contact with osteoclasts, TRAP$^+$ osteoclasts were identified. Then, osteoblasts that were and were not in direct contact with osteoclasts were manually identified. Last, ALP expression area of the selected osteoblasts was quantified using ImageJ.

Statistics
All measurements were collected in at least triplicate and expressed as means ± SD. P values were calculated using the t test and one-way analysis of variance (ANOVA) with post hoc Bonferroni test in statistical package for the social sciences (SPSS, IBM). ANOVA was used to assess significance, with $*P < 0.05$ and $**P < 0.01$.

SUPPLEMENTARY MATERIALS
Supplementary material for this article is available at http://advances.sciencemag.org/cgi/content/full/7/4/eabd6495/DC1

View/request a protocol for this paper from Bio-protocol.

REFERENCES AND NOTES
1. J. Bilezikian, T. J. Martin, T. L. Clemens, C. J. Rosen, *Principles of Bone Biology* (Elsevier, ed. 4, 2019).
2. S. Melmed, R. J. Auchus, A. B. Goldfine, R. J. Koenig, C. J. Rosen, *Williams Textbook of Endocrinology* (Elsevier Inc., ed. 14, 2019).
3. L. J. Raggatt, N. C. Partridge, Cellular and molecular mechanisms of bone remodeling. *J. Biol. Chem.* **285**, 25103–25108 (2010).
4. B. F. Boyce, L. Xing, Functions of RANKL/RANK/OPG in bone modeling and remodeling. *Arch. Biochem. Biophys.* **473**, 139–146 (2008).
5. A. M. Parfitt, The cellular basis of bone remodeling: The quantum concept reexamined in light of recent advances in the cell biology of bone. *Calcif. Tissue Int.* **36** (Suppl. 1), S37–S45 (1984).
6. B. Langdahl, S. Ferrari, D. W. Dempster, Bone modeling and remodeling: Potential as therapeutic targets for the treatment of osteoporosis. *Ther. Adv. Musculoskelet. Dis.* **8**, 225–235 (2016).
7. S. C. Manolagas, R. L. Jilka, Bone marrow, cytokines, and bone remodeling—emerging insights into the pathophysiology of osteoporosis. *N. Eng. J. Med.* **332**, 305–311 (1995).
8. S. J. Morrison, D. T. Scadden, The bone marrow niche for haematopoietic stem cells. *Nature* **505**, 327–334 (2014).
9. P. I. Croucher, M. M. McDonald, T. J. Martin, Bone metastasis: The importance of the neighbourhood. *Nat. Rev. Cancer* **16**, 373–386 (2016).

10. E. F. Eriksen, Normal and pathological remodeling of human trabecular bone: Three dimensional reconstruction of the remodeling sequence in normals and in metabolic bone disease. *Endocr. Rev.* **7**, 379–408 (1986).

11. K. W. Rogers, A. F. Schier, Morphogen gradients: From generation to interpretation. *Annu. Rev. Cell Dev. Biol.* **27**, 377–407 (2011).

12. A. Vortkamp, Skeleton morphogenesis: Defining the skeletal elements. *Curr. Biol.* **7**, R104–R107 (1997).

13. O. Wartlick, A. Kicheva, M. Gonzalez-Gaitan, Morphogen gradient formation. *Cold Spring Harb. Perspect. Biol.* **1**, a001255 (2009).

14. L. Kunz, T. Schroeder, A 3D tissue-wide digital imaging pipeline for quantitation of secreted molecules shows absence of CXCL12 gradients in bone marrow. *Cell Stem Cell* **25**, 846–854.e4 (2019).

15. T. Bellido, J. Delgado-Calle, Ex vivo organ cultures as models to study bone biology. *JBMR Plus* **4**, 10.1002/jbm4.10345, (2020).

16. G. L. Koons, M. Diba, A. G. Mikos, Materials design for bone-tissue engineering. *Nat. Rev. Mater.* **5**, 584–603 (2020).

17. N. Kohli, S. Ho, S. J. Brown, P. Sawadkar, V. Sharma, M. Snow, E. Garcia-Gareta, Bone remodelling in vitro: Where are we headed?: A review on the current understanding of physiological bone remodelling and inflammation and the strategies for testing biomaterials in vitro. *Bone* **110**, 38–46 (2018).

18. M. Rumpler, T. Wurger, P. Roschger, E. Zwettler, I. Sturmlechner, P. Altmann, P. Fratzl, M. J. Rogers, K. Klaushofer, Osteoclasts on bone and dentin in vitro: Mechanism of trail formation and comparison of resorption behavior. *Calcif. Tissue Int.* **93**, 526–539 (2013).

19. E. Gruskin, B. A. Doll, F. W. Futrell, J. P. Schmitz, J. O. Hollinger, Demineralized bone matrix in bone repair: History and use. *Adv. Drug Deliv. Rev.* **64**, 1063–1077 (2012).

20. N. Reznikov, M. Bilton, L. Lari, M. M. Stevens, R. Kroger, Fractal-like hierarchical organization of bone begins at the nanoscale. *Science* **360**, eaao2189 (2018).

21. J. Lee, M. J. Cuddihy, N. A. Kotov, Three-dimensional cell culture matrices: State of the art. *Tissue Eng. Part B Rev.* **14**, 61–86 (2008).

22. G. Borciani, G. Montalbano, N. Baldini, G. Cerqueni, C. Vitale-Brovarone, G. Ciapetti, Co-culture systems of osteoblasts and osteoclasts: Simulating in vitro bone remodeling in regenerative approaches. *Acta Biomater.* **108**, 22–45 (2020).

23. X. Ren, Q. Zhou, D. Foulad, A. S. Tiffany, M. J. Dewey, D. Bischoff, T. A. Miller, R. R. Reid, T. C. He, D. T. Yamaguchi, B. A. C. Harley, J. C. Lee, Osteoprotegerin reduces osteoclast resorption activity without affecting osteogenesis on nanoparticulate mineralized collagen scaffolds. *Sci. Adv.* **5**, eaaw4991 (2019).

24. L. L. Bennink, Y. Li, B. Kim, I. J. Shin, B. H. San, M. Zangari, D. Yoon, S. M. Yu, Visualizing collagen proteolysis by peptide hybridization: From 3D cell culture to in vivo imaging. *Biomaterials* **183**, 67–76 (2018).

25. X. Chen, O. Nadiarynkh, S. Plotnikov, P. J. Campagnola, Second harmonic generation microscopy for quantitative analysis of collagen fibrillar structure. *Nat. Protoc.* **7**, 654–669 (2012).

26. S. Boonrungsiman, E. Gentleman, R. Carzaniga, N. D. Evans, D. W. McComb, A. E. Porter, M. M. Stevens, The role of intracellular calcium phosphate in osteoblast-mediated bone apatite formation. *Proc. Natl. Acad. Sci. U.S.A.* **109**, 14170–14175 (2012).

27. S. C. Miller, L. de Saint-Georges, B. M. Bowman, W. S. Jee, Bone lining cells: Structure and function. *Scanning Microsc.* **3**, 953–960 (1989).

28. L. I. Plotkin, T. Bellido, Beyond gap junctions: Connexin43 and bone cell signaling. *Bone* **52**, 157–166 (2013).

29. I. Matic, B. G. Matthews, X. Wang, N. A. Dyment, D. L. Worthley, D. W. Rowe, D. Grcevic, I. Kalajzic, Quiescent bone lining cells are a major source of osteoblasts during adulthood. *Stem Cells* **34**, 2930–2942 (2016).

30. I. D. Jansen, J. A. Vermeer, V. Bloemen, J. Stap, V. Everts, Osteoclast fusion and fission. *Calcif. Tissue Int.* **90**, 515–522 (2012).

31. C. E. Jacome-Galarza, G. I. Percin, J. T. Muller, E. Mass, T. Lazarov, J. Eitler, M. Rauner, V. K. Yadav, L. Crozet, M. Bohm, P. L. Loyher, G. Karsenty, C. Waskow, F. Geissmann, Developmental origin, functional maintenance and genetic rescue of osteoclasts. *Nature* **568**, 541–545 (2019).

32. N. A. Sims, T. J. Martin, Osteoclasts provide coupling signals to osteoblast lineage cells through multiple mechanisms. *Annu. Rev. Physiol.* **82**, 507–529 (2020).

33. M. Furuya, J. Kikuta, S. Fujimori, S. Seno, H. Maeda, M. Shirazaki, M. Uenaka, H. Mizuno, Y. Iwamoto, A. Morimoto, K. Hashimoto, T. Ito, Y. Isogai, M. Kashii, T. Kaito, S. Ohba, U. Chung, A. C. Lichtler, K. Kikuchi, H. Matsuda, H. Yoshikawa, M. Ishii, Direct cell–cell contact between mature osteoblasts and osteoclasts dynamically controls their functions in vivo. *Nat. Commun.* **9**, 300 (2018).

34. V. Raina, Normal osteoid tissue. *J. Clin. Pathol.* **25**, 229–232 (1972).

35. J. S. Choi, B. A. Harley, Marrow-inspired matrix cues rapidly affect early fate decisions of hematopoietic stem and progenitor cells. *Sci. Adv.* **3**, e1600455 (2017).

36. T. Bai, J. Li, A. Sinclair, S. Imren, F. Merriam, F. Sun, M. B. O'Kelly, C. Nourigat, P. Jain, J. J. Delrow, R. S. Basom, H.-C. Hung, P. Zhang, B. Li, S. Heimfeld, S. Jiang, C. Delaney, Expansion of primitive human hematopoietic stem cells by culture in a zwitterionic hydrogel. *Nat. Med.* **25**, 1566–1575 (2019).

37. X. Li, L. Wang, Y. Fan, Q. Feng, F. Z. Cui, F. Watari, Nanostructured scaffolds for bone tissue engineering. *J. Biomed. Mater. Res. A* **101**, 2424–2435 (2013).

38. J.-G. Kwak, J. Lee, Thermoresponsive inverted colloidal crystal hydrogel scaffolds for lymphoid tissue engineering. *Adv. Healthc. Mater.* **9**, e1901556 (2020).

39. D. B. Chou, V. Frismantas, Y. Milton, R. David, P. Pop-Damkov, D. Ferguson, A. MacDonald, O. V. Bolukbasi, C. E. Joyce, L. S. M. Teixeira, A. Rech, A. Jiang, E. Calamari, S. Jalili-Firoozinezhad, B. A. Furlong, L. R. O'Sullivan, C. F. Ng, Y. Choe, S. Marquez, K. C. Myers, O. K. Weinberg, R. P. Hasserjian, R. Novak, O. Levy, R. Prantil-Baun, C. D. Novina, A. Shimamura, L. Ewart, D. E. Ingber, On-chip recapitulation of clinical bone marrow toxicities and patient-specific pathophysiology. *Nat. Biomed. Eng.* **4**, 394–406 (2020).

40. D. E. Glaser, M. B. Curtis, P. A. Sariano, Z. A. Rollins, B. S. Shergill, A. Anand, A. M. Deely, V. S. Shirure, L. Anderson, J. M. Lowen, N. R. Ng, K. Weilbaecher, D. C. Link, S. C. George, Organ-on-a-chip model of vascularized human bone marrow niches. *bioRxiv* 2020.2004.2017.039339 , (2020).

41. S. Méndez-Ferrer, T. V. Michurina, F. Ferraro, A. R. Mazloom, B. D. Macarthur, S. A. Lira, D. T. Scadden, A. Ma'ayan, G. N. Enikolopov, P. S. Frenette, Mesenchymal and haematopoietic stem cells form a unique bone marrow niche. *Nature* **466**, 829–834 (2010).

42. X. Chen, Z. Wang, N. Duan, G. Zhu, E. M. Schwarz, C. Xie, Osteoblast-osteoclast interactions. *Connect. Tissue Res.* **59**, 99–107 (2018).

43. L. F. Bonewald, The amazing osteocyte. *J. Bone Miner. Res.* **26**, 229–238 (2011).

44. J. Xiong, M. Onal, R. L. Jilka, R. S. Weinstein, S. C. Manolagas, C. A. O'Brien, Matrix-embedded cells control osteoclast formation. *Nat. Med.* **17**, 1235–1241 (2011).

45. T. Nakashima, M. Hayashi, T. Fukunaga, K. Kurata, M. Oh-Hora, J. Q. Feng, L. F. Bonewald, T. Kodama, A. Wutz, E. F. Wagner, J. M. Penninger, H. Takayanagi, Evidence for osteocyte regulation of bone homeostasis through RANKL expression. *Nat. Med.* **17**, 1231–1234 (2011).

46. A. G. Robling, C. H. Turner, Mechanical signaling for bone modeling and remodeling. *Crit. Rev. Eukaryot. Gene Expr.* **19**, 319–338 (2009).

47. Y. Li, G. Toraldo, A. Li, X. Yang, H. Zhang, W. P. Qian, M. N. Weitzmann, B cells and T cells are critical for the preservation of bone homeostasis and attainment of peak bone mass in vivo. *Blood* **109**, 3839–3848 (2007).

48. B. L. McClune, N. S. Majhail, Osteoporosis after stem cell transplantation. *Curr. Osteoporos. Rep.* **11**, 305–310 (2013).

49. B. Parekkadan, J. M. Milwid, Mesenchymal stem cells as therapeutics. *Annu. Rev. Biomed. Eng.* **12**, 87–117 (2010).

50. D. Li, Z. Yang, Z. Wei, P. Kang, Efficacy of bisphosphonates in the treatment of femoral head osteonecrosis: A PRISMA-compliant meta-analysis of animal studies and clinical trials. *Sci. Rep.* **8**, 1450 (2018).

Citation: Y. Park, E. Cheong, J.-G. Kwak, R. Carpenter, J.-H. Shim, J. Lee, Trabecular bone organoid model for studying the regulation of localized bone remodeling. *Sci. Adv.* **7**, eabd6495 (2021).

Science Advances

Trabecular bone organoid model for studying the regulation of localized bone remodeling

Yongkuk ParkEugene CheongJun-Goo KwakRyan CarpenterJae-Hyuck ShimJungwoo Lee

Use of this article is subject to the Terms of service